Design Trade-offs in Zero-Emission Agricultural Tractors: A Thermodynamic Comparison of Battery and Hydrogen Powertrains

Barbara Mendecka[a], Chiara Putano Bisti[a], Laura Tribioli[a], Leonardo Federici[a] and Simone Lombardi[a]

[a] *Niccolò Cusano University, Rome, Italy, barbara.mendecka@unicusano.it CA*

Abstract:
The decarbonization of agricultural machinery represents a critical challenge for reducing greenhouse gas emissions in energy-intensive farming operations. While electrification strategies are increasingly investigated in on-road transport, comparative thermodynamic and environmental assessments of alternative tractor powertrains under realistic field workloads remain limited. This study presents an integrated evaluation of alternative compact tractor architectures, comparing a battery-electric configuration, two hydrogen fuel-cell hybrid configurations with 350 bar and 700 bar onboard storage, and a conventional diesel internal combustion baseline.
A forward quasi-static vehicle model is used to reproduce representative agricultural duty cycles, including traction dynamics, terrain slope effects, auxiliary consumption, and implement-driven Power Take-Off demand. The powertrain configurations are parameterized to reflect component sizing constraints, onboard storage characteristics, conversion efficiencies, and hydrogen refuelling requirements. The analysis combines tank-to-field and well-to-field exergy indicators with operational and embodied greenhouse gas emissions, allowing energy consumption, exergy efficiency, storage trade-offs, and life-cycle-related environmental impacts to be evaluated within a unified framework tailored to agricultural operation.
The results reveal distinct architecture-dependent trade-offs. The battery-electric configuration achieves the highest tank-to-field exergy efficiency, with values up to about 0.89, due to the direct use of electrical energy and the high efficiency of the electric drivetrain. The fuel-cell hybrid configurations show intermediate exergy efficiencies, around 0.44–0.47, and provide lower onboard storage volume than the battery-electric solution, particularly at 700 bar. However, this compactness is obtained at the cost of higher hydrogen refuelling energy demand and additional conversion losses. The diesel configuration exhibits the lowest exergy efficiency and the highest greenhouse gas emissions. Under the assumed green hydrogen pathway, the fuel-cell configurations achieve the lowest total emissions per cultivated hectare, while the battery-electric configuration remains penalized by the embodied contribution of the battery pack.
By integrating thermodynamic, environmental, and architectural considerations, this work provides a methodological basis for comparing alternative tractor powertrains under realistic agricultural workloads. The proposed framework supports the design of next-generation low-carbon agricultural machinery and can be extended to scenarios involving renewable on-farm energy production, hydrogen refuelling infrastructure, and uncertainty-based assessment of energy carrier pathways.

Keywords:
Thermodynamics, Energy, ECOS Conference, Exergy, Sustainability.

1. Introduction

Recent years have seen a growing interest in the electrification and decarbonization of agricultural and heavy-duty vehicles, driven by increasingly stringent environmental regulations and the need to reduce greenhouse gas emissions. The agricultural sector plays a significant role in this transition, as

conventional diesel-powered tractors are a major source of greenhouse gases and air pollutants, with direct impacts on environmental quality and human health [1].

From a system-level perspective, several studies have compared different drivetrain configurations in terms of energy performance and economic viability. Maggini et al. [2] highlighted that while diesel technologies remain cost-effective in many scenarios, fuel cell electric vehicles (FCEVs) can become competitive for medium-to-long driving ranges when considering total cost of ownership (TCO) and operational conditions. These findings underline the importance of duty cycle characteristics in determining the optimal propulsion technology.

Focusing on the agricultural sector, electrification presents additional challenges due to highly variable and non-standard operating conditions. Agricultural tractors operate under combined traction and power take-off (PTO) loads, resulting in strongly transient and application-specific power demands. Martini et al. [3] demonstrated that hybrid fuel cell–battery configurations can effectively handle such variability, improving system efficiency and reducing emissions compared to conventional diesel systems.

Beyond energy performance, the environmental impact of alternative powertrains must be evaluated over the entire life cycle. Martelli et al. [1] performed a cradle-to-grave life cycle assessment of diesel and fuel cell-powered orchard tractors, showing that fuel cell systems can reduce climate change impacts by more than 30%, with even higher reductions in other environmental categories. However, the results strongly depend on the hydrogen production pathway, highlighting the need for integrated system-level and environmental analyses.

Hydrogen-based systems introduce additional complexity related to storage, compression, and supply chain efficiency. High-pressure hydrogen storage and multi-stage compression systems significantly affect the overall system performance and efficiency, as discussed in studies on hydrogen storage technologies and compression processes [4–6]. These aspects are particularly relevant for off-road applications, where refuelling infrastructure and operational flexibility are critical.

In parallel, exergy-based approaches have been increasingly adopted to provide a rigorous thermodynamic assessment of energy conversion systems. Exergy analysis enables the identification of irreversibilities and inefficiencies within complex powertrains and has been widely applied to fuels, hydrogen systems, and energy conversion processes [7, 8]. Compared to conventional energy-based metrics, exergy provides deeper insight into the quality of energy flows and the real potential for system optimization.

Despite the growing body of literature addressing techno-economic, environmental, and thermodynamic aspects, these analyses are often conducted separately. Furthermore, many studies rely on standardized driving cycles, which are not representative of real agricultural applications. In practice, agricultural machinery operates under highly specific duty cycles, where load variability, auxiliary systems, and PTO usage significantly influence system performance.

Unlike conventional approaches, the present work employs experimentally derived agricultural duty cycles, including both traction and PTO loads, enabling a more realistic representation of actual operating conditions. Building on previous work by the authors [9], the analysis integrates vehicle simulation, exergy-based performance indicators, and environmental metrics within a unified framework.

In this context, while BEV solutions are often considered a viable pathway for decarbonization, their application in agricultural machinery is constrained by limitations in energy density, operational autonomy, and charging infrastructure. Conversely, hydrogen-based systems offer potential advantages in terms of refuelling time, energy density, and suitability for high-duty applications, making them particularly attractive for agricultural scenarios.

Therefore, the present work aims to provide a comparative thermodynamic and environmental assessment of alternative tractor powertrains under realistic field operations. By combining exergy-based analysis with system-level and environmental considerations, the study addresses the existing gap in the literature and provides a comprehensive evaluation of electric and hydrogen-based agricultural

vehicles.

2. Powertrain Description

In this study, three powertrain configurations have been modeled and investigated: a conventional diesel internal combustion engine (ICE) powertrain, a battery electric powertrain (BEV) and a hydrogen fuel cell electric powertrain (FCEV). In all cases, the key powertrain components are represented by means of quasi-static efficiency maps, which relate the operating point of each component to its energy consumption or efficiency, avoiding the computational overhead of dynamic component models while retaining sufficient accuracy for energy analysis over driving cycles.

2.1. ICE Model

The tractor is equipped with a diesel internal combustion engine with a rated power output of 28.8 kW. The engine model is derived from a unit available in the literature [10] and included in the authors' internal database, which has been appropriately scaled to match a nominal power of 28.8 kW, representative of typical agricultural tractor applications. The resulting steady-state performance maps provide a consistent characterization of fuel consumption across the operating range in terms of torque and rotational speed. The overall ICE powertrain configuration is illustrated in Fig. 1.

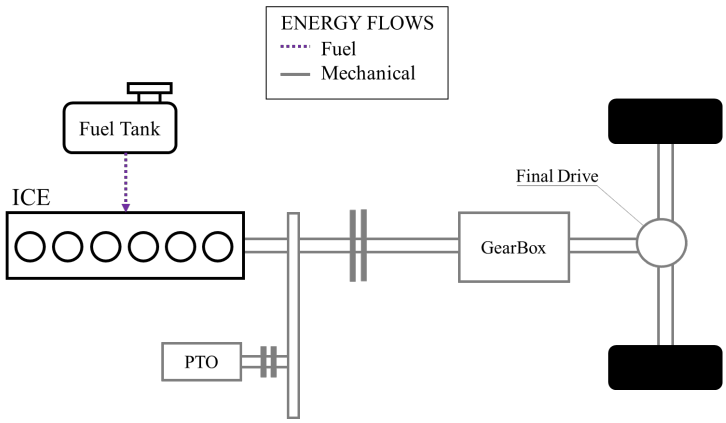

Figure 1: Schematic representation of the tractor ICE configuration

Specifically, the fuel mass flow rate $\dot{m}_f$ is expressed as a function of the requested torque T_{req} and rotational speed ω_{req}:

$$\dot{m}_f = f(T_{\text{req}}, \omega_{\text{req}}) \tag{1}$$

This functional relationship is represented through a two-dimensional map interpolated over a discretized grid of operating points. The corresponding engine performance map is shown in Fig. 2.

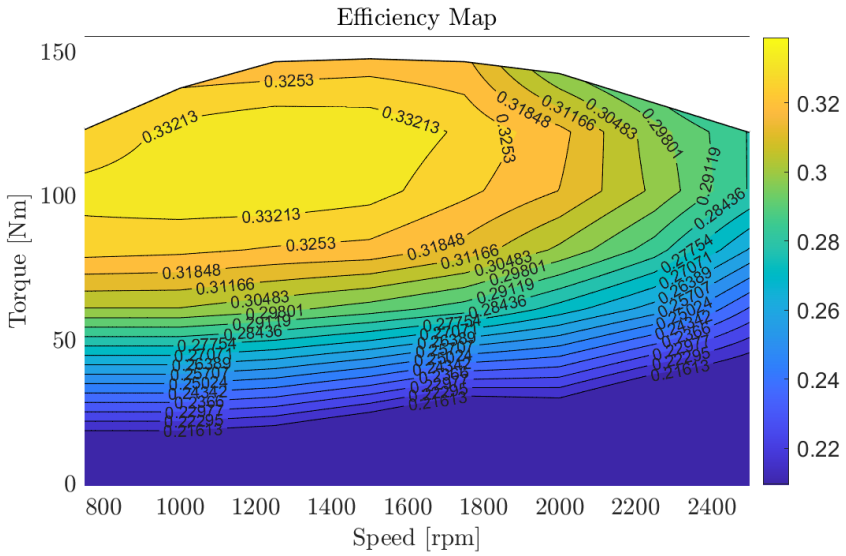

Figure 2: Internal Combustion Engine Efficiency Map

2.2. Electric Motor Model

The electric motor (EM) is modeled within the powertrain block together with the inverter and driveline, accounting for the main physical constraints of the traction system. The mechanical power required at the motor shaft is derived from the wheel demand by considering the overall transmission efficiency. The overall BEV powertrain configuration is illustrated in Fig. 3.

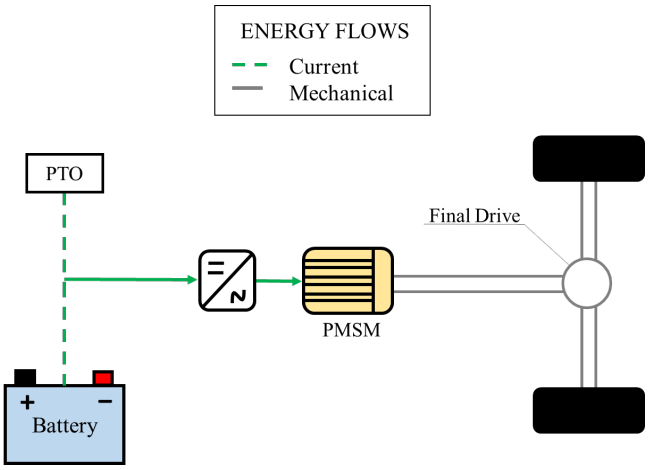

Figure 3: Schematic representation of the tractor BEV configuration

The electric motor (EM) adopted in both the BEV and fuel cell configurations is based on a Danfoss EM-PMI375-T800 permanent magnet machine. This motor has been appropriately scaled to deliver torque and speed characteristics consistent with the requirements of agricultural tractor applications. The resulting efficiency map, derived from the original machine and adapted to the target operating range, is used to represent the motor behavior across its working domain [11]. In particular, the motor efficiency η_{EM} is expressed as:

$$\eta_{\mathrm{EM}} = f(T_{\mathrm{EM}}, \omega_{\mathrm{EM}}) \tag{2}$$

The corresponding electric motor efficiency map is shown in Fig. 4.

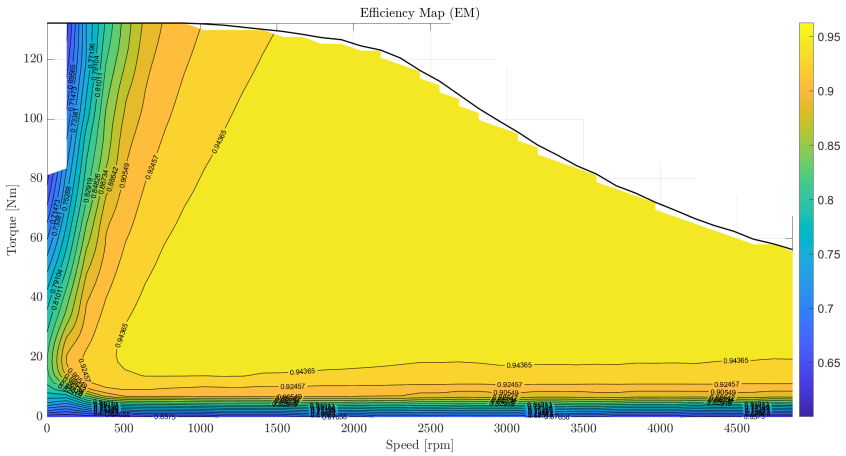

Figure 4: Electric motor efficiency map

Based on the torque-speed operating envelope adopted in this study, the electric motor delivers a maximum torque of approximately 110 Nm and reaches a peak power of about 30 kW at intermediate rotational speeds. This behavior is consistent with typical traction electric machines, characterized by a constant torque region at low speeds followed by a constant power region.
The drivetrain is modeled through a constant efficiency, accounting for mechanical losses between the motor shaft and the wheels. Consistently with typical agricultural tractor transmissions, a constant efficiency is assumed for each component of the driveline.
The inverter is not explicitly modeled; its losses are implicitly included within the overall efficiency of the electric powertrain.
Regenerative braking is not considered in the present model. Agricultural tractors typically operate at low speeds and under continuous traction load, resulting in limited opportunities for energy recovery. Therefore, neglecting regenerative braking has a negligible impact on the overall energy consumption estimation.

Table 1: Characteristics of the electric motor investigated in this study.

Specification	Traction Electric Motor
Model / Type	Danfoss EM-PMI375-T800 scaled
Power	30 kW @ 110 Nm
Voltage [V]	200 V DC - 400V AC

2.3. Battery Model

The primary objective of the battery model is to estimate the evolution of the State of Charge (SoC) during operation. To this end, a second-order Equivalent Circuit Model (ECM) is adopted, providing a suitable compromise between computational efficiency and accuracy in capturing the battery's dynamic behavior. The model evaluates the instantaneous battery voltage, V_{batt}, as a function of the battery current I_{batt}, the open-circuit voltage $OCV(\text{SoC}, T)$, and the internal resistive and dynamic contributions of the circuit elements.

$$V_{\text{bat}} = OCV - R_0 I_{\text{bat}} - V_{RC1} - V_{RC2} \tag{3}$$

where OCV is the open-circuit voltage and R_0 is the ohmic internal resistance. The dynamic behavior

of the RC branches is governed by:

$$\frac{dV_{RC1}}{dt} = -\frac{1}{R_1 C_1} V_{RC1} + \frac{1}{C_1} I_{\text{bat}} \tag{4}$$

$$\frac{dV_{RC2}}{dt} = -\frac{1}{R_2 C_2} V_{RC2} + \frac{1}{C_2} I_{\text{bat}} \tag{5}$$

The SOC is updated using a coulomb counting approach:

$$\frac{d\text{SOC}}{dt} = -\frac{I_{\text{bat}}}{Q_{\text{bat}}} \tag{6}$$

where Q_{bat} denotes the nominal battery capacity.
Both the open-circuit voltage and the internal resistances are modeled as functions of SOC, allowing the nonlinear dependence of battery behavior on its charge level to be captured. The temperature influence is neglected, as the battery is assumed to operate under controlled thermal conditions at a constant temperature of 25°C.
From a thermal perspective, heat generation is attributed to ohmic losses in the internal resistive elements:

$$\dot{Q}_{\text{gen}} = I_{\text{bat}}^2 \left(R_0 + R_1 + R_2\right) \tag{7}$$

while heat dissipation to the environment is modeled via convection:

$$\dot{Q}_{\text{loss}} = hA \left(T_{\text{bat}} - T_{\text{amb}}\right) \tag{8}$$

where h is the convective heat transfer coefficient, A is the battery surface area, and T_{amb} is the ambient temperature.
The battery pack considered in this study is composed of cylindrical lithium-ion cells with lithium iron phosphate (LFP) chemistry, each characterized by a nominal capacity of 14 Ah.
The main characteristics of the adopted cells are summarized in Table 2.

Table 2: Characteristics of the battery cells investigated in this study.

Specification	32140 (LFP)
Chemistry	LFP
Cathode	$LiFePO_4$
Anode	Graphite
Voltage Range [V]	2.5–3.7
Nominal Capacity [Ah]	14
Standard Discharge Current [A]	8
Max. Continuous Discharge [A]	60
Max. Continuous Charge [A]	14
Geometry	Cylindrical
Dimensions D×H [mm]	32×140
Mass [kg]	380

The pack is properly sized to achieve a total energy capacity of 50 kWh, ensuring sufficient energy autonomy for the considered agricultural duty cycles while maintaining realistic packaging constraints for compact tractor applications.
The sizing procedure accounts for both energy and power requirements, resulting in a configuration that guarantees sufficient autonomy while maintaining the battery within safe operating limits in terms of current and SOC range. The adopted modeling approach allows capturing both steady-state and transient electrical behavior, making it suitable for system-level simulations of the overall powertrain.

2.4. Fuel Cell Model

The powertrain has been sized according to the vehicle energy demand and operating strategy requirements. The system consists of a 30 kW fuel cell system, a reduced-capacity battery pack of 3.3 kWh, and an electric traction motor identical to the one used in the baseline BEV configuration, modeled using the same efficiency maps in order to ensure consistency and comparability between the two architectures. An overview of the fuel cell powertrain configuration is provided in Fig. 5.

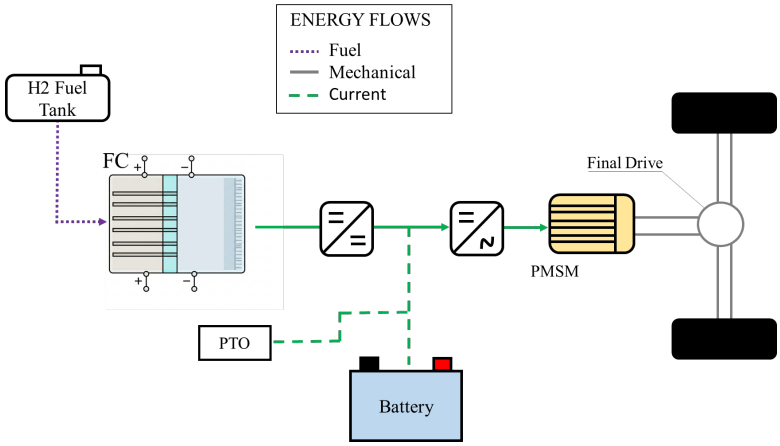

Figure 5: Hybrid fuel cell powertrain configuration.

The fuel cell system is based on a scaled Ballard stack model [12], adapted to meet the required power range of the application. Its electrical output and hydrogen consumption are derived from a polarization-based performance map as a function of the requested power P_{req}: The efficiency behavior of the fuel cell as a function of the output power is reported in Fig. 6.

$$\dot{m}_{\text{H}_2} = f(P_{\text{req}}) \tag{9}$$

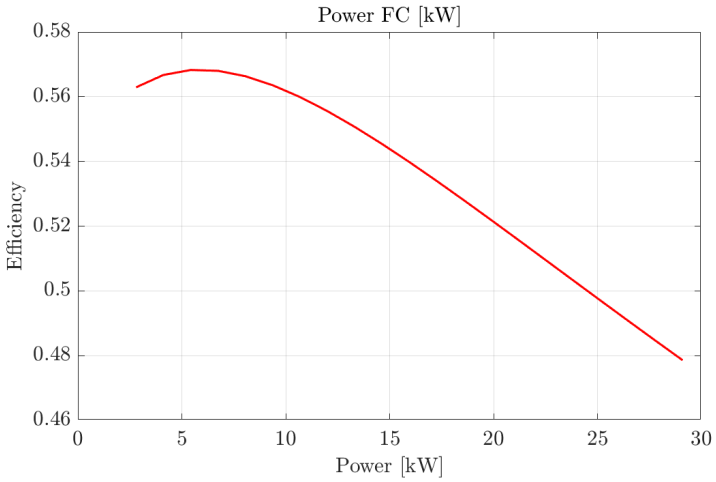

Figure 6: Fuel Cell Efficiency curve as a Function of Power

The battery is used as a buffer element to handle transient loads and to support the fuel cell during dynamic operating conditions. The state of charge (SOC) is actively managed within a restricted operating window between 40% and 70%, which represents a design choice aimed at preserving battery lifetime and ensuring optimal hybridization strategy performance.
To further ensure battery durability and long-term operation, the SOC operating window is constrained to avoid deep discharge and overcharge conditions, which are known to accelerate degradation phenomena such as capacity fade and resistance increase. Within this range, the battery operates mainly as a power buffer, reducing stress associated with high C-rate cycling.

The DC/DC converter is modeled using a constant efficiency approach, without detailed switching dynamics, in order to reduce model complexity while preserving realistic energy flow losses.
Overall, the energy management strategy ensures that the fuel cell operates primarily in its efficient region, while the battery compensates for fast load variations and peak power demands.

3. Model Description

A forward simulation framework is adopted to describe the interaction among driver behaviour, vehicle longitudinal dynamics, and powertrain components under transient conditions. In this approach, a virtual driver follows a predefined speed trajectory and generates control inputs that propagate through the drivetrain, allowing the determination of instantaneous operating conditions and energy flows within the system.
In contrast to backward quasi-static methods, the forward formulation captures the causal relationship between driver input and vehicle response, providing a more representative description of real operating conditions. This makes the approach suitable for applications requiring time-domain consistency, such as real-time simulations and hardware-in-the-loop environments.
At the component level, a quasi-static representation is employed. Since the overall energy balance is predominantly influenced by the battery state-of-charge (SOC) evolution, higher-frequency dynamics can be neglected without significantly affecting the accuracy of the results. This assumption enables a reduction in model complexity while preserving fidelity at the system level.
The modelling framework is organized into three main subsystems:

- **Driver block** — determines the control actions, namely acceleration $\alpha(t)$ and braking $\beta(t)$, through a PI controller based on the tracking error;
- **Vehicle block** — evaluates the longitudinal motion and computes the required wheel power $P_{\text{wheel}}(t)$;
- **Powertrain block** — delivers the requested power while updating the internal states of the components (e.g., SOC and temperatures) according to the selected energy management strategy.

3.1. Driver Block

The Driver block generates the control signal $u(t)$ through a PI controller acting on the velocity tracking error:

$$u(t) = K_P\, e(t) + K_I \int_0^t e(\tau)\, \mathrm{d}\tau + K_G\, \gamma(t) \tag{10}$$

where the error is defined as:

$$e(t) = v_{\text{des}}(t) - v_{\text{eff}}(t) \tag{11}$$

The controller parameters have been tuned to ensure accurate tracking of the reference speed profile under the considered operating conditions. In particular, a feedforward contribution associated with the road grade $\gamma(t)$ has been included in order to compensate for slope-induced load variations, as the simulated driving cycles are characterized by non-zero and time-varying gradients.
The effectiveness of the control strategy is evaluated by comparing the desired and actual vehicle speed profiles, together with the corresponding acceleration and braking signals. These quantities are reported in Fig. 7.

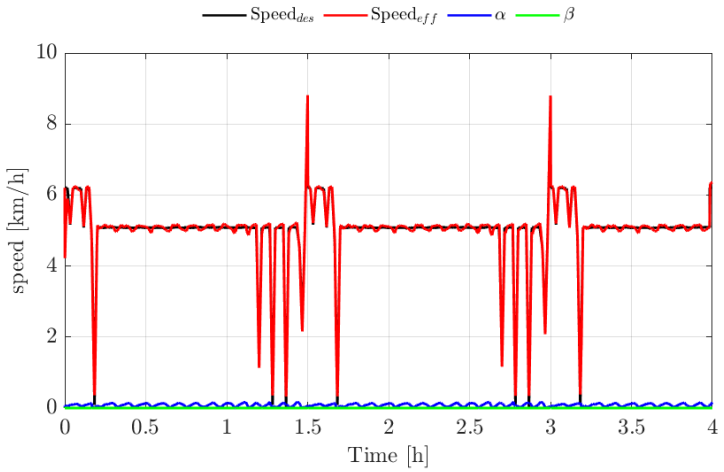

Figure 7: Comparison between reference and actual vehicle speed, along with the corresponding acceleration and braking signals.

3.2. Vehicle Block

The Vehicle block determines the vehicle speed $v_{\text{eff}}(t)$ by integrating the longitudinal acceleration $a_{\text{eff}}(t)$, which is fed back to the Driver block. The acceleration is obtained from the force balance along the longitudinal direction:

$$a_{\text{eff}}(t) = \frac{F_T(t) - F_r(t)}{k_{\text{in}}\, M} \tag{12}$$

where $F_T(t)$ represents the traction force at the wheels and $F_r(t)$ accounts for the total resistive forces. The overall vehicle mass is defined as the sum of a baseline chassis mass, the implement mass, the ballast mass, and the mass contribution of the selected powertrain architecture:

$$M = m_v + m_e + m_b + m_{PT} \tag{13}$$

where m_{PT} represents the additional mass associated with the considered powertrain configuration. Specifically, different values are assumed for the ICE, BEV, and FCHEV architectures as reported in Table 3.
The term k_{in} represents the contribution of rotating inertias within the drivetrain [13].
The resistive force is expressed as:

$$F_r(t) = \frac{1}{2}\,\rho_a\, C_d\, A_f\, v_{\text{eff}}^2(t) + k_{\text{roll}}\, M\, g\, \cos\theta(t) + M\, g\, \sin\theta(t) \tag{14}$$

where ρ_a is the air density and $\theta(t)$ is the road slope angle. The remaining parameters are listed in Table 3.

The vehicle considered in this work is a compact agricultural tractor developed within the BRIC Compact Tractor 4.0 project [14, 15]. The design is tailored for vineyard and orchard operations, with a track width below 1150 mm and a maximum height of 1600 mm.
The main geometric and inertial properties, assumed unchanged across the different powertrain configurations, are summarized in Table 3.

Table 3: Main vehicle parameters common to all powertrain architectures.

Symbol	Description	Value
m_v	Vehicle mass (bare)	2300 kg
m_e	Implement/equipment mass	400 kg
m_b	Ballast mass	100 kg
m_{ICE}	ICE powertrain mass	150 kg
m_{BEV}	BEV powertrain mass	450 kg
m_{FC}	FCHEV powertrain mass	200 kg
r_r	Wheel rolling radius	484 mm
A_f	Frontal area	1.75 m^2
C_d	Aerodynamic drag coefficient	1.5
k_{roll}	Rolling resistance coeff.	0.08

4. Thermodynamic and Environmental Assessment Framework

The comparison among the investigated tractor powertrain architectures was carried out through an integrated thermodynamic, environmental and stochastic assessment framework. Four powertrain configurations were considered: a conventional diesel internal combustion engine tractor (ICE), a battery electric tractor (BEV), and two fuel-cell hybrid electric tractor configurations supplied with compressed hydrogen at 350 bar and 700 bar, respectively.

The framework was coupled with the quasi-static vehicle simulation model developed for the agricultural duty cycles. For each cycle, the model provides the useful mechanical energy delivered to the wheels and to the Power Take-Off (PTO), together with the corresponding diesel, battery or hydrogen consumption. Since the adopted vehicle model does not include temperature-resolved component submodels, the thermodynamic assessment was performed at system level using exergy balance indicators rather than local entropy generation analysis. This allows a consistent comparison among different energy carriers and conversion technologies while remaining coherent with the available simulation outputs.

4.1. System-level exergy analysis

The useful exergy output was assumed equal to the useful mechanical energy delivered by the tractor during field operation. Accordingly, the useful exergy was defined as:

$$Ex_{\text{useful}} = E_{\text{wheel}} + E_{\text{PTO}} \tag{15}$$

where E_{wheel} and E_{PTO} are the mechanical energy contributions delivered to the wheels and to the PTO, respectively.

A tank-to-field (TF) boundary was first adopted to evaluate the onboard thermodynamic performance of each architecture. In this formulation, the input exergy is defined at the vehicle boundary, according to the energy carrier stored onboard:

$$Ex_{\text{input}}^{\text{TF}} = \begin{cases} m_f \, ex_{\text{diesel}}^{ch} & \text{ICE} \\ E_{\text{batt}} & \text{BEV} \\ m_{H_2} \left(ex_{H_2}^{ch} + ex_{H_2}^{phys} \right) & \text{FCHEV} \end{cases} \tag{16}$$

where m_f is the diesel fuel mass, E_{batt} is the electrical energy delivered by the battery, m_{H_2} is the consumed hydrogen mass, and ex^{ch} and ex^{phys} are the specific chemical and physical exergy terms.

For diesel fuel, the physical exergy contribution was neglected because storage occurs close to ambient conditions. The specific chemical exergy of diesel was evaluated from its lower heating value through an empirical exergy factor [16]:

$$ex^{ch}_{\text{diesel}} = \beta_{\text{diesel}} LHV_{\text{diesel}} \tag{17}$$

with $\beta_{\text{diesel}} = 1.06$ and $LHV_{\text{diesel}} = 42.8$ MJ kg^{-1}.
For hydrogen, the specific chemical exergy was assumed equal to:

$$ex^{ch}_{H_2} = 117.11 \text{ MJ kg}^{-1} \tag{18}$$

as reported in exergetic life-cycle studies of hydrogen systems [17]. The physical exergy associated with compressed storage was explicitly evaluated as:

$$ex^{phys}_{H_2} = (h - h_0) - T_0(s - s_0) \tag{19}$$

where h and s are the specific enthalpy and entropy of hydrogen at the storage condition, while h_0 and s_0 are the corresponding values at the reference environment. The dead state was defined as $T_0 = 298.15$ K and $p_0 = 1.01325$ bar. Hydrogen thermodynamic properties were evaluated using real-gas property relations implemented in CoolProp [**?**].
The tank-to-field exergy efficiency was then calculated as:

$$\eta^{\text{TF}}_{\text{ex}} = \frac{Ex_{\text{useful}}}{Ex^{\text{TF}}_{\text{input}}} \tag{20}$$

and the difference between supplied and useful exergy was used as a system-level indicator of irreversibility-related losses:

$$Ex^{\text{TF}}_{\text{loss}} = Ex^{\text{TF}}_{\text{input}} - Ex_{\text{useful}} \tag{21}$$

4.2. Well-to-field exergy boundary

In addition to the vehicle-boundary formulation, a well-to-field (WF) exergy perspective was introduced to account for the upstream processes required to supply each energy carrier. This boundary is analogous to the well-to-wheel approach commonly adopted in vehicle studies, but it is adapted here to agricultural operation, where the useful output is field work rather than road traction [1, 3, 18].
The well-to-field exergy input was defined as:

$$Ex^{\text{WF}}_{\text{input}} = Ex^{\text{TF}}_{\text{input}} + Ex_{\text{up}} \tag{22}$$

where Ex_{up} represents the upstream exergy required for fuel production, electricity generation, battery charging, hydrogen production and hydrogen refuelling.
The adopted WF formulation was:

$$Ex^{\text{WF}}_{\text{input}} = \begin{cases} \dfrac{m_f \, ex^{ch}_{\text{diesel}}}{\eta_{\text{ex,diesel}}} & \text{ICE} \\ \dfrac{E_{\text{batt}}}{\eta_{\text{ch}} \, \eta_{\text{ex,elec}}} & \text{BEV} \\ m_{H_2} \left(\dfrac{ex^{ch}_{H_2}}{\eta_{\text{ex},H_2}} + \dfrac{w_{\text{HRS}}}{\eta_{\text{ex,elec}}} + ex^{phys}_{H_2} \right) & \text{FCHEV} \end{cases} \tag{23}$$

where $\eta_{\text{ex,diesel}}$ accounts for diesel refining and distribution, η_{ch} is the battery charging efficiency, $\eta_{\text{ex,elec}}$ is the exergy efficiency of the electricity supply pathway, η_{ex,H_2} represents the hydrogen production pathway, and w_{HRS} is the specific electrical energy demand of the hydrogen refuelling station.

The corresponding well-to-field exergy efficiency was defined as:

$$\eta_{\mathrm{ex}}^{\mathrm{WF}} = \frac{Ex_{\mathrm{useful}}}{Ex_{\mathrm{input}}^{\mathrm{WF}}} \tag{24}$$

This dual-boundary formulation allows the intrinsic onboard performance of each tractor architecture to be separated from the upstream exergy penalty associated with the selected energy carrier.

4.3. Hydrogen refuelling station model

For the FCHEV configurations, the hydrogen refuelling station was modelled explicitly in order to estimate the specific electrical energy required to deliver hydrogen at the selected pressure level. Two refuelling scenarios were considered: H35, representative of 350 bar onboard storage, and H70, representative of 700 bar onboard storage.

The model includes three main subsystems: hydrogen multistage compression, hydrogen precooling through a heat exchanger located in the pressure control unit (PCU), and a two-stage vapour-compression refrigeration cycle supplying the cooling duty. The refuelling cases were defined consistently with SAE J2601-type pressure classes and dispenser temperature categories [19, 20]. The precooling unit was modelled following the thermodynamic structure discussed by Elgowainy et al. [21]. For each refuelling case, the filling time was calculated from the average pressure ramp rate:

$$t_{\mathrm{fill}} = \frac{P_{\mathrm{final}} - P_{\mathrm{initial}}}{APRR} \tag{25}$$

where pressures are expressed in MPa and $APRR$ in MPa min^{-1}. The average hydrogen mass flow rate was then obtained as:

$$\dot{m}_{H_2} = \frac{m_{\mathrm{fill}}}{t_{\mathrm{fill}}} \tag{26}$$

The filled hydrogen mass was calculated from the real-gas density variation inside a fixed-volume tank:

$$m_{\mathrm{fill}} = (\rho_f - \rho_i)\, V_{\mathrm{tank}} \tag{27}$$

where ρ_i and ρ_f are the initial and final hydrogen densities evaluated at the tank temperature and pressure, and V_{tank} is the tank volume. In the present analysis, the tank volume was sized to contain 5 kg of hydrogen at the nominal pressure level, namely 350 bar for H35 and 700 bar for H70.

Hydrogen compression was modelled as a multistage process with uniform pressure ratio among stages:

$$\beta = \left(\frac{p_{\mathrm{out}}}{p_{\mathrm{in}}}\right)^{1/N} \tag{28}$$

where N is the number of compression stages. For each stage, the isentropic outlet state was calculated as:

$$h_{2s} = h(p_2, s_1) \tag{29}$$

and the actual outlet enthalpy was obtained from the compressor isentropic efficiency:

$$h_2 = h_1 + \frac{h_{2s} - h_1}{\eta_{\mathrm{is}}} \tag{30}$$

The shaft power of each compression stage was therefore:

$$\dot{W}_{\mathrm{comp},i} = \dot{m}_{H_2}(h_2 - h_1) \tag{31}$$

and the total electrical compression power was calculated as:

$$\dot{W}_{\mathrm{comp,el}} = \frac{\sum_i \dot{W}_{\mathrm{comp},i}}{\eta_{\mathrm{mech,el}}} \tag{32}$$

Intercooling between stages and aftercooling at the compressor outlet were included. The corresponding thermal loads were calculated from the hydrogen enthalpy decrease across each cooling process. The PCU cooling duty was evaluated from the hydrogen enthalpy change between the inlet and outlet of the dispenser heat exchanger:

$$\dot{Q}_{\mathrm{PCU}} = \dot{m}_{H_2} \left(h_{\mathrm{in}} - h_{\mathrm{out}}\right) \tag{33}$$

where the outlet temperature corresponds to the selected dispenser temperature class. This thermal duty was supplied by a two-stage vapour-compression refrigeration cycle using R404A as refrigerant. The refrigeration model includes low-pressure and high-pressure compression, interstage cooling, condensation, expansion and evaporation.
The coefficient of performance of the refrigeration system was calculated as:

$$COP = \frac{\dot{Q}_{\mathrm{PCU}}}{\dot{W}_{\mathrm{ref,el}}} \tag{34}$$

and the specific electricity consumption of the refuelling station was obtained as:

$$SEC_{\mathrm{HRS}} = \frac{\dot{W}_{\mathrm{comp,el}} + \dot{W}_{\mathrm{ref,el}}}{\dot{m}_{H_2}} \tag{35}$$

expressed in kWh $\mathrm{kg}_{H_2}^{-1}$. In the baseline implementation, additional station overheads were neglected in order to isolate the contribution of compression and precooling. However, the model structure allows daily overhead electricity demand to be included as an additional term normalized by the daily dispensed hydrogen mass.
The HRS model therefore provides pressure-specific values of w_{HRS} for the WF exergy analysis, distinguishing the 350 bar and 700 bar hydrogen pathways not only in terms of onboard physical exergy, but also in terms of refuelling station electricity demand.

4.4. Environmental assessment

The environmental assessment was performed by combining operational greenhouse gas emissions with the embodied impact of the main powertrain components. Operational emissions were calculated on a well-to-field basis according to the energy carrier consumed during each duty cycle. The environmental model builds on previous LCA-based approaches for agricultural and road vehicle powertrains [1, 14, 18].
For the ICE configuration, operational emissions were calculated from the consumed diesel mass:

$$GHG_{\mathrm{op,ICE}} = m_f \, EF_{\mathrm{diesel}} \tag{36}$$

where EF_{diesel} is the selected diesel emission factor.
For the BEV configuration, operational emissions were calculated from the battery energy demand:

$$GHG_{\mathrm{op,BEV}} = E_{\mathrm{batt}} \, EF_{\mathrm{elec}} \tag{37}$$

where EF_{elec} represents the carbon intensity of the electricity supply pathway.
For the FCHEV configurations, operational emissions were calculated from the consumed hydrogen mass and the selected hydrogen production pathway:

$$GHG_{\mathrm{op,FCHEV}} = m_{H_2} \, EF_{H_2} + m_{H_2} \, w_{\mathrm{HRS}} \, EF_{\mathrm{elec}} \tag{38}$$

where EF_{H_2} is the pathway-dependent hydrogen carbon intensity and the second term accounts for the electricity required by the refuelling station when modelled separately.

Table 4: Main operational emission factors adopted in the environmental assessment.

Energy carrier / pathway	Emission factor	Unit
Diesel, tank-to-field combustion	3.24	$\mathrm{kgCO_2\ kg_{fuel}^{-1}}$
Diesel, well-to-field supply	3.74–3.82	$\mathrm{kgCO_2\ kg_{fuel}^{-1}}$
Electricity, EU mix	0.40–0.42	$\mathrm{kgCO_2\ kWh^{-1}}$
Electricity, renewable supply	0.02–0.05	$\mathrm{kgCO_2\ kWh^{-1}}$
Hydrogen, renewable electrolysis	0.7–2.8	$\mathrm{kgCO_2\ kg_{H_2}^{-1}}$
Hydrogen, grey SMR	7.5–13.0	$\mathrm{kgCO_2\ kg_{H_2}^{-1}}$
Hydrogen, blue SMR/ATR with CCUS	0.2–4.8	$\mathrm{kgCO_2\ kg_{H_2}^{-1}}$

Hydrogen was not treated as a single fuel pathway. Instead, the uncertainty analysis included ten hydrogen production routes, following the hydrogen colour classification and carbon-intensity ranges reported by Incer-Valverde et al. [22]. The adopted values are summarized in Table 5.

Table 5: Hydrogen production pathways and carbon-intensity ranges adopted in the uncertainty analysis.

Hydrogen pathway	Main production route	CI [$\mathrm{kgCO_2eq\ kg_{H_2}^{-1}}$]
Green	Electrolysis supplied by dedicated RES	0.7–2.8
Blue	SMR/ATR with carbon capture and storage	0.2–4.8
Grey	SMR without carbon capture	7.5–13.0
Black	Bituminous coal gasification	18–25
Brown	Lignite gasification	18–25
Turquoise	Methane pyrolysis with solid carbon by-product	1.9–4.8
Pink	Electrolysis supplied by nuclear electricity	0.3–0.6
Red	High-temperature nuclear thermochemical route	0.05–0.20
Yellow	Electrolysis supplied by dedicated photovoltaic electricity	1.0–1.7
Orange	Electrolysis supplied by average grid electricity	10–40

Although selected representative hydrogen pathways are discussed in the deterministic baseline, the stochastic analysis includes all ten hydrogen pathways reported in Table 5. This allows the FCHEV results to be interpreted as a function of the hydrogen supply route rather than as a single fixed technology assumption.

4.5. Component manufacturing impact

In addition to operational emissions, the embodied impact associated with the manufacturing of the main powertrain components was considered. A simplified component-based approach was adopted, focusing on the subsystems that differ among the investigated architectures.
The embodied impact was calculated as:

$$I_{\mathrm{emb}} = \sum_i m_i \epsilon_i \tag{39}$$

where m_i is the mass of the i-th component and ϵ_i is the corresponding specific impact factor. For battery systems, a capacity-based formulation was used:

$$I_{\mathrm{bat}} = E_{\mathrm{bat,inst}} \epsilon_{\mathrm{bat}} \tag{40}$$

where $E_{\mathrm{bat,inst}}$ is the installed battery capacity and ϵ_{bat} is the specific battery manufacturing impact per unit capacity.

The analysis included the internal combustion engine, electric motor, battery pack, fuel cell system, power electronics and compressed hydrogen storage tank. For hydrogen storage, different tank assumptions were adopted for the 350 bar and 700 bar cases, allowing the mass and embodied impact of the storage system to be pressure-dependent. The tank assumptions were based on literature data for Type III and Type IV compressed hydrogen storage systems [**?**]. Fuel-cell manufacturing impacts were based on recent cradle-to-gate PEMFC data [23], while battery manufacturing impacts were derived from vehicle LCA studies [18].

Table 6: Specific environmental impact factors adopted for component manufacturing.

Component	Impact factor	Unit
Battery pack	80–131	$\mathrm{kgCO_2\ kWh^{-1}}$
Fuel cell system	60–90	$\mathrm{kgCO_2\ kW^{-1}}$
Hydrogen tank, 350 bar	15	$\mathrm{kgCO_2\ kg_{tank}^{-1}}$
Hydrogen tank, 700 bar	18–25	$\mathrm{kgCO_2\ kg_{tank}^{-1}}$
ICE engine	5–10	$\mathrm{kgCO_2\ kg^{-1}}$

The total environmental impact of each configuration was then calculated as:

$$GHG_{\mathrm{tot}} = GHG_{\mathrm{op}} + I_{\mathrm{emb,alloc}} \tag{41}$$

where $I_{\mathrm{emb,alloc}}$ is the embodied impact allocated to the considered duty cycle according to the selected functional basis, either operating hours or cultivated area.

4.6. Uncertainty and sensitivity analysis

To account for the uncertainty of key parameters, a Monte Carlo analysis was implemented. The uncertain parameters include energy carrier carbon intensities, component manufacturing factors, hydrogen pathway emissions, storage tank assumptions, component lifetime and selected drivetrain efficiencies. Latin Hypercube Sampling was used when available; otherwise, random sampling was adopted. For each sampled set of parameters, the thermodynamic and environmental indicators were recalculated. The results were reported in terms of median values and 5th–95th percentile intervals. In addition, a one-at-a-time sensitivity analysis was performed to identify the parameters with the largest influence on the well-to-field exergy efficiency and total greenhouse gas emissions. This stochastic formulation allows the comparison among ICE, BEV and FCHEV architectures to be interpreted not only through deterministic baseline values, but also through uncertainty ranges associated with the main technological and supply-chain assumptions.

5. Case study

To evaluate the performance of the different powertrain architectures under realistic operating conditions, three representative agricultural duty cycles are considered. Each cycle reproduces a specific field operation typically performed by compact tractors in vineyard and orchard applications:

- Duty cycle 1 – *Shredding* (mulching operations)
- Duty cycle 2 – *Treatments* (spraying operations)
- Duty cycle 3 – *Soil tillage* (high-load field operations)

The three cycles differ in terms of speed profile, terrain gradient, load intensity and power-demand dynamics, ranging from relatively steady conditions with quasi-constant PTO load (shredding) to highly transient operations with intermittent implement demand (treatments) and to high-traction operations with lower variability (soil tillage). Together, they capture the main characteristics of agricultural workloads, which are generally defined by low operating speeds, frequent load transients and combined traction and implement power demands.
The duty cycles are derived from experimental data collected during real agricultural operations. Each cycle includes a speed–time profile representative of typical phases such as field work, manoeuvring and transfer. To improve the accuracy of the load estimation, terrain effects are explicitly considered through grade profiles, since operations are often carried out on uneven or sloped terrain which significantly affects traction demand and energy consumption. In addition to traction, the power demand associated with the Power Take-Off (PTO) system is included, because a significant fraction of the total energy consumption in agricultural machinery is related to implement operation. The resulting profiles therefore represent complete operating cycles rather than simple driving cycles.
Figure 8 shows the three duty cycles adopted in this study.

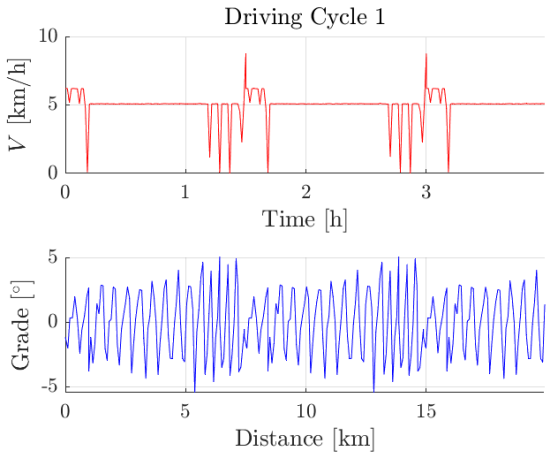

(a) Cycle 1 – Shredding

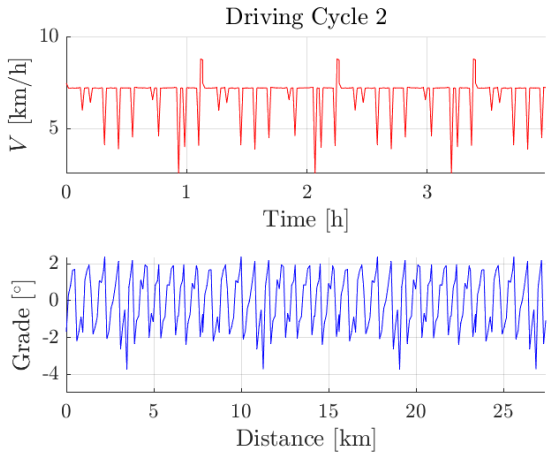

(b) Cycle 2 – Treatments

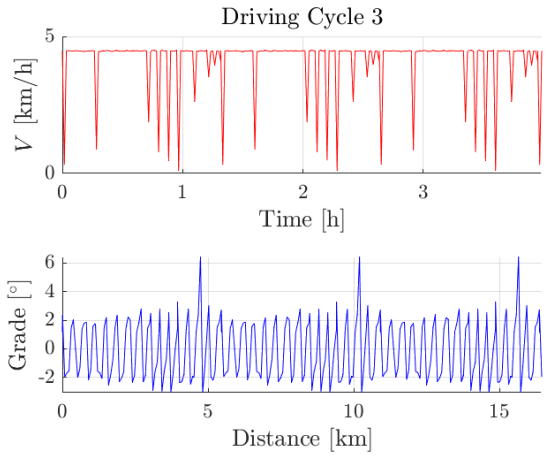

(c) Cycle 3 – Soil tillage

Figure 8: Agricultural duty cycles adopted in the analysis.

Each duty cycle is associated with a representative cultivated area, derived from the simulated operating conditions. The three duty cycles correspond to 2.3 ha (Cycle 1), 3.2 ha (Cycle 2) and 1.90 ha (Cycle 3). These values are used to normalize the results on a per-hectare basis, which represents the most relevant functional unit for agricultural applications and enables a consistent comparison of

energy, exergy and environmental indicators across operations of different extent.
Table 7 summarizes the main characteristics of the three cycles, including duration, cultivated area and corresponding onboard fuel or energy demand for each powertrain configuration.

6. Simulation results

The simulation results highlight the performance of the three powertrain configurations under the considered agricultural duty cycles. All architectures successfully complete the assigned tasks, confirming that the component sizing is adequate for the required operating conditions.
Table 7 summarizes the total onboard energy demand over the three duty cycles. The systems are sized to guarantee at least 4 h of continuous operation, corresponding to a typical half-day working session. Across all cycles, the BEV configuration consistently exhibits the lowest energy consumption, followed by the FCHEV and the conventional ICE. The BEV requires between 25.40 and 41.69 kWh depending on the duty cycle, while the FCHEV demand ranges from 43.51 to 74.55 kWh, approximately 1.7–1.8 times higher than the BEV. The ICE configuration shows the highest consumption levels, ranging from 96.74 to 134.40 kWh, i.e. about 3.2–3.9 times higher than the BEV.
The superior performance of the BEV is primarily due to the high efficiency of the electric drivetrain and the absence of intermediate energy conversion processes. The FCHEV exhibits a higher energy demand due to additional losses associated with hydrogen conversion in the fuel cell system and power electronics: although the fuel cell operates at relatively high efficiency, the overall system efficiency remains lower than that of a direct battery-electric configuration.
From an operational perspective, the soil tillage cycle (Cycle 3) is characterized by the highest specific energy demand per hectare, due to higher traction loads and lower average speeds, although its total per-cycle consumption is lower than Cycle 2 because a smaller area is covered. The treatment cycle (Cycle 2) exhibits the highest total energy demand, with more transient behaviour and frequent load variations due to intermittent implement operation. The shredding cycle (Cycle 1) represents an intermediate condition with a quasi-steady PTO load.
It should be noted that the energy comparison refers to onboard energy demand (tank-to-field), while upstream contributions are discussed separately in the exergy and environmental analysis.

Table 7: Characterization of the agricultural duty cycles and corresponding energy demand for different powertrain architectures.

Parameter	**Duty cycle 1**	**Duty cycle 2**	**Duty cycle 3**
Operation type	Shredding	Treatments	Soil tillage
Duration	4 h	4 h	4 h
Cultivated area	2.29 ha	3.16 ha	1.89 ha
Average working rate	0.55 ha h^{-1}	0.75 ha h^{-1}	0.46 ha h^{-1}
Onboard energy demand			
Diesel consumption (ICE)	8.14 kg (9.78 L)	11.31 kg (13.59 L)	8.26 kg (9.93 L)
Hydrogen consumption (FCHEV)	1.54 kg	2.24 kg	1.31 kg
Battery energy (BEV)	28.74 kWh	41.69 kWh	25.40 kWh
Equivalent onboard energy demand (kWh)			
BEV	28.74 kWh	41.69 kWh	25.40 kWh
FCHEV	51.34 kWh	74.55 kWh	43.51 kWh
ICE	96.74 kWh	134.40 kWh	98.17 kWh

From a system integration perspective, the different energy demands translate into significantly different onboard storage requirements. The BEV configuration is equipped with a 50.1 kWh LFP battery pack, corresponding to an estimated mass of approximately 385 kg and a volume of about 210 L. In

contrast, the FCHEV requires hydrogen storage on the order of a few kilograms. Hydrogen storage was evaluated for both 350 bar (H35) and 700 bar (H70) configurations. The tank volume was calculated assuming a nominal storage capacity of 5 kg of hydrogen at 20°C. Based on real-gas hydrogen properties, the resulting internal tank volume is 211.4 L for the H35 configuration and 126.0 L for the H70 configuration. These values correspond to SAE J2601 CHSS Capacity Category C for the H35 case (174–248.6 L, 4.18–5.97 kg H_2) and Capacity Category B for the H70 case (99.4–174 L, 4–7 kg H_2).

For the most demanding duty cycle, the required hydrogen mass is approximately 2.24 kg (see Table 7). This corresponds to an estimated internal storage volume of about 97 L for the H35 configuration and about 58 L for the H70 configuration. Therefore, the 700 bar configuration reduces the required storage volume by approximately 40 % compared with the 350 bar case.

However, this increased compactness is achieved at the expense of higher refuelling energy demand. The hydrogen refuelling station (HRS) model shows that the specific electricity consumption ranges from 1.98 to 2.20 kWh $kg_{H_2}^{-1}$ for the H35 cases and from 2.55 to 2.77 kWh $kg_{H_2}^{-1}$ for the H70 cases, depending on the dispenser temperature class. This increase is mainly associated with the higher compression work required to reach the 700 bar storage level, while the contribution of the precooling unit remains of similar magnitude for both configurations. As a result, the total refuelling energy demand is systematically higher for the H70 case.

Table 8: Hydrogen storage and refuelling station results for H35 and H70 configurations.

Parameter	H35 configuration	H70 configuration
Nominal storage pressure	350 bar	700 bar
Tank volume for 5 kg H_2	211.4 L	126.0 L
Estimated volume for 2.24 kg H_2	97 L	58 L
Compression energy	1.82 kWh $kg_{H_2}^{-1}$	2.39 kWh $kg_{H_2}^{-1}$
PCU electricity demand	0.16–0.38 kWh $kg_{H_2}^{-1}$	0.17–0.39 kWh $kg_{H_2}^{-1}$
Total HRS electricity demand	1.98–2.20 kWh $kg_{H_2}^{-1}$	2.55–2.77 kWh $kg_{H_2}^{-1}$

Overall, the comparison highlights a clear trade-off between energy efficiency, storage compactness and system complexity. The BEV provides the lowest energy demand but requires a larger onboard storage mass. The FCHEV offers higher energy density, particularly at 700 bar, but at the cost of additional energy losses associated with hydrogen conversion and refuelling processes.

The following figures provide a more detailed view of the dynamic behaviour of the electrified architectures during the selected duty cycle. In particular, the power split and battery state-of-charge profiles are analysed to verify the consistency of the component sizing and the adopted energy management strategy.

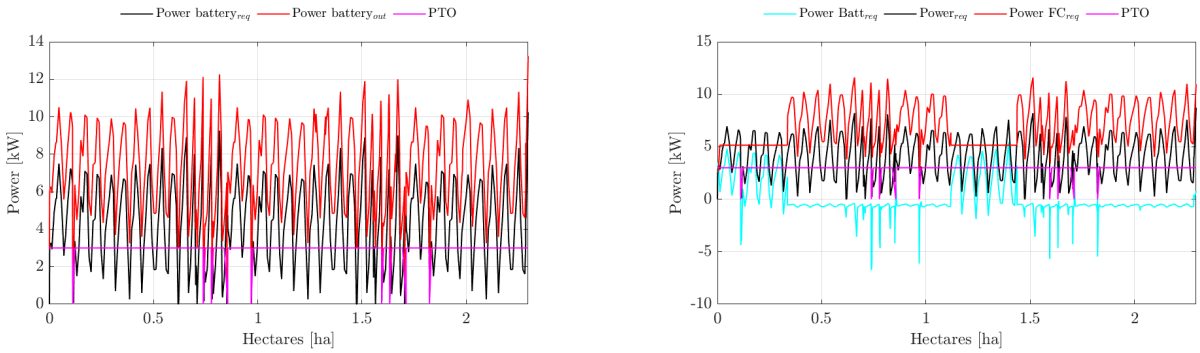

(a) BEV power split

(b) FCHEV power split

Figure 9: Power split comparison between BEV and FCHEV architectures during Duty cycle 1.

The power split profiles for the BEV and FCHEV architectures during Duty cycle 1 are shown in Fig. 9. In both cases, the PTO load represents a quasi-constant baseline demand, onto which the time-varying traction power is superimposed. In the BEV configuration, the battery directly supplies both traction and PTO loads, and the resulting power profile follows the instantaneous load demand of the vehicle. In the FCHEV configuration, the fuel cell operates at a smoother and more stable power level, while the battery acts as a buffer to compensate for fast load variations. This behaviour is consistent with the adopted energy management strategy and reduces the exposure of the fuel cell to high-frequency transients.

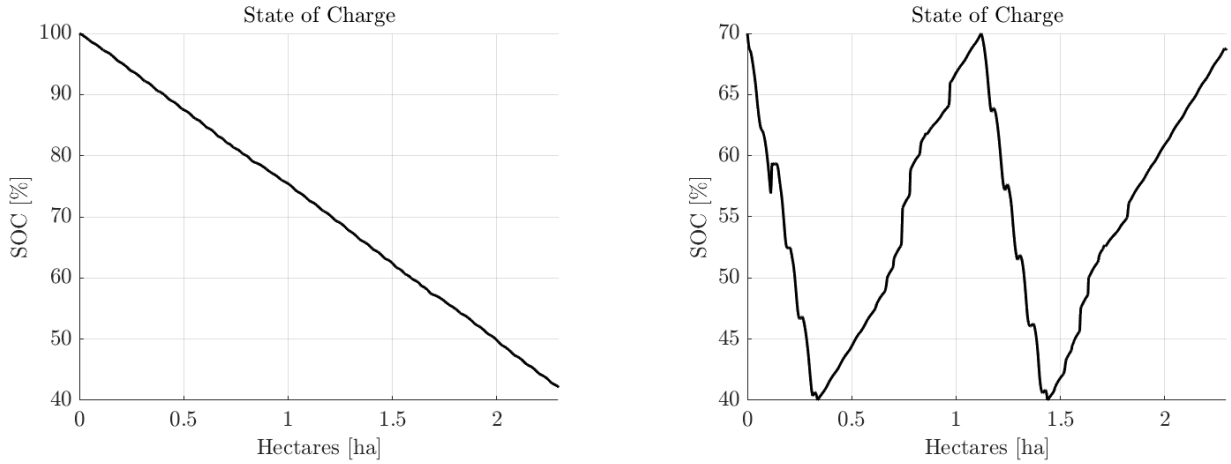

(a) BEV – State of Charge evolution

(b) FCHEV – Battery State of Charge evolution

Figure 10: State of Charge evolution for BEV and FCHEV architectures during duty cycle 1.

The battery State of Charge evolution confirms that the selected storage capacities are sufficient to complete the duty cycle while maintaining an adequate energy margin. In the BEV case, the SoC decreases progressively because the battery is the only onboard energy source. In the FCHEV case, the battery SoC remains within the prescribed operating window, since the fuel cell provides the average power demand and the battery compensates for transient load variations. Negative battery power values correspond to charging phases driven by the fuel cell during low-demand periods.
Figure 11 summarizes the exergy efficiencies and the balance between input and useful exergy for all configurations.

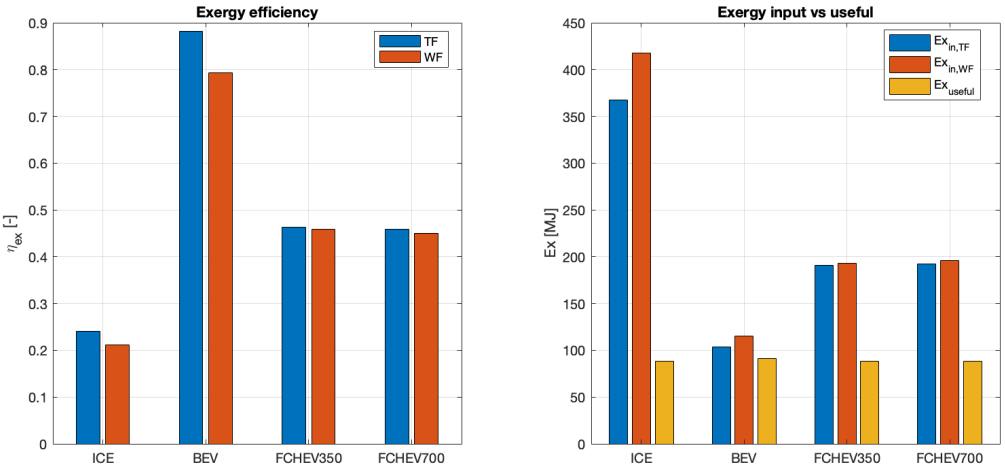

Figure 11: Exergy efficiency and exergy balance for the investigated powertrain architectures (duty cycle 1).

The BEV configuration exhibits the highest exergy efficiency, reaching $\eta_{\mathrm{ex,TF}} \approx 0.88$ and $\eta_{\mathrm{ex,WF}} \approx 0.79$. This behaviour is directly related to the absence of intermediate energy conversion processes and to the high efficiency of the electric drivetrain. The FCHEV configurations show intermediate efficiencies, with $\eta_{\mathrm{ex,WF}} \approx 0.45$ for both 350 and 700 bar storage. The difference between the two pressure levels is small (about 0.5–0.8 percentage points), indicating that the additional compression work required for 700 bar storage only slightly penalizes the overall system efficiency. The ICE configuration exhibits the lowest efficiency, with $\eta_{\mathrm{ex,WF}} \approx 0.21$, due to the intrinsic irreversibilities associated with combustion processes. Despite a comparable useful exergy output across all architectures, the ICE requires a significantly higher exergy input, highlighting the inefficiency of thermochemical conversion.
In the following, results are primarily discussed on a cultivated-area basis ($\mathrm{kgCO_2eq\,ha^{-1}}$ and $\mathrm{MJ\,ha^{-1}}$), which represents the most relevant functional unit for agricultural applications. Absolute values per duty cycle are also reported for completeness.

Table 9: Thermodynamic and environmental performance indicators of the investigated powertrain architectures.

Duty cycle	Powertrain	$\eta_{\mathrm{ex}}^{\mathrm{TF}}$ [-]	$\eta_{\mathrm{ex}}^{\mathrm{WF}}$ [-]	$Ex_{\mathrm{input}}^{\mathrm{TF}}$ [MJ ha^{-1}]	$Ex_{\mathrm{input}}^{\mathrm{WF}}$ [MJ ha^{-1}]	GHG_{op} [kgCO$_2$eq ha^{-1}]	GHG_{tot} [kgCO$_2$eq ha^{-1}]
1	ICE	0.2408	0.2119	160.06	181.88	13.195	13.352
1	BEV	0.8813	0.7931	45.07	50.07	3.825	5.075
1	FCHEV350	0.4632	0.4581	83.05	83.98	1.460	1.901
1	FCHEV700	0.4586	0.4503	83.89	85.44	1.572	2.000
2	ICE	0.2522	0.2220	161.49	183.52	13.313	13.471
2	BEV	0.8920	0.8028	47.48	52.76	4.030	5.280
2	FCHEV350	0.4692	0.4640	87.57	88.55	1.540	2.040
2	FCHEV700	0.4645	0.4561	88.45	90.08	1.657	2.140
3	ICE	0.1891	0.1664	197.08	223.95	16.247	16.404
3	BEV	0.8049	0.7244	48.33	53.70	4.102	5.352
3	FCHEV350	0.4408	0.4360	85.39	86.35	1.501	1.922
3	FCHEV700	0.4365	0.4285	86.25	87.85	1.616	2.026

Table 9 summarizes the main thermodynamic and environmental indicators obtained for the investigated powertrain architectures. The results are reported on a cultivated-area basis in order to provide

a direct comparison among the three agricultural duty cycles.
From a thermodynamic perspective, the BEV configuration shows the highest exergy efficiency in all cycles, with tank-to-field values ranging from 0.805 to 0.892. This behaviour is mainly associated with the direct use of electrical energy and with the high efficiency of the electric drivetrain. The FCHEV configurations exhibit intermediate exergy efficiencies, with values around 0.44–0.47, due to the additional conversion step from hydrogen to electricity in the fuel cell system. The ICE configuration shows the lowest exergy efficiency, with tank-to-field values between 0.189 and 0.252, reflecting the intrinsic irreversibilities of combustion-based power generation.
The well-to-field formulation reduces the exergy efficiency of all architectures because upstream energy supply processes are included. The effect is particularly evident for the ICE and BEV configurations, where diesel supply and electricity generation affect the overall balance. For the FCHEV cases, the difference between tank-to-field and well-to-field efficiency is smaller in the adopted reference case, because green hydrogen was assumed and the upstream exergy penalty was limited to the refuelling station electricity demand.
The comparison between FCHEV350 and FCHEV700 shows that the 700 bar configuration is slightly less efficient than the 350 bar configuration. This is due to the higher physical exergy at the higher pressure level and to the higher refuelling station energy demand associated with compression to 700 bar. However, the difference remains limited, and the main advantage of the 700 bar case is the reduction in onboard storage volume.
From an environmental perspective, the ICE architecture presents the highest greenhouse gas emissions, with total values between 13.35 and 16.40 $\mathrm{kgCO_2eq\,ha^{-1}}$. The BEV significantly reduces operational emissions, but its total impact is increased by the embodied contribution of the battery pack, reaching approximately 5.1–5.4 $\mathrm{kgCO_2eq\,ha^{-1}}$. The FCHEV configurations show the lowest total emissions in the green hydrogen scenario, with values around 1.9–2.1 $\mathrm{kgCO_2eq\,ha^{-1}}$.
The embodied contribution was allocated to each operation assuming a 10-year life cycle and the corresponding operating lifetime of each component. This allocation allows the manufacturing burden of the main powertrain components to be consistently combined with the operational emissions of each duty cycle. In the BEV case, the battery pack dominates the embodied contribution, while in the FCHEV configurations the impact is distributed among the fuel cell system, the buffer battery and the hydrogen storage system.
Overall, the results indicate that the BEV architecture provides the best thermodynamic performance, whereas the FCHEV configurations can achieve the lowest greenhouse gas emissions when low-carbon hydrogen is assumed. The ICE architecture remains penalized both thermodynamically and environmentally. This confirms the importance of evaluating alternative tractor powertrains through a combined tank-to-field, well-to-field and life-cycle perspective.
Finally, uncertainty and sensitivity analyses were performed to evaluate the robustness of the deterministic results. The Monte Carlo analysis accounts for variability in hydrogen carbon intensity, electricity carbon intensity, embodied manufacturing factors, component lifetime and selected efficiency parameters. The corresponding results are reported below.
Figure 12 presents the breakdown of greenhouse gas emissions for each architecture, distinguishing between operational and embodied contributions.

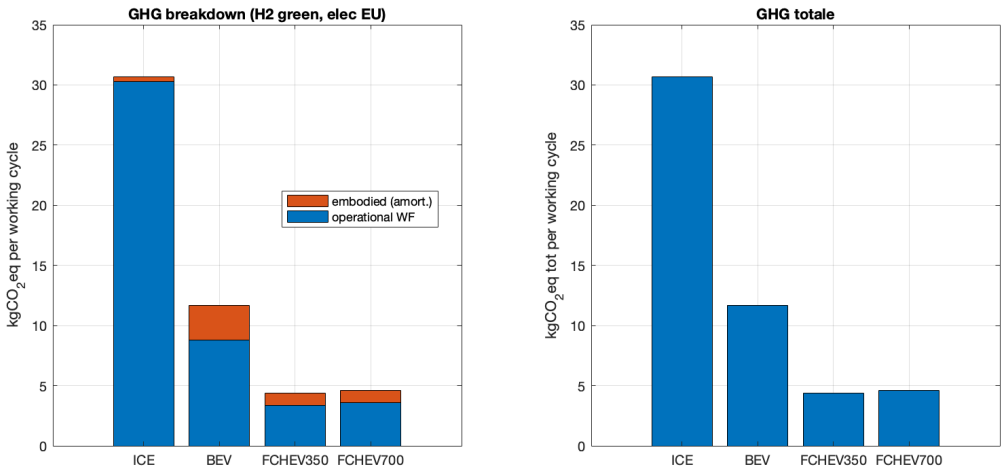

Figure 12: GHG emissions breakdown and total emissions (duty cycle 1, H_2 green, electricity EU mix).

The ICE configuration shows the highest emissions, dominated by the operational phase, with total values between 29 and 41 $kgCO_2eq$ per duty cycle across the three operations. The BEV significantly reduces operational emissions; however, its total impact remains influenced by the embodied contribution of the battery system. The FCHEV configurations achieve the lowest total emissions under the assumed green hydrogen pathway, with values between 3.5 and 6.1 $kgCO_2eq$ per cycle. In this case, the environmental burden is more evenly distributed between operational and embodied contributions. The robustness of these results is further assessed through a Monte Carlo analysis, as shown in Fig. 13.

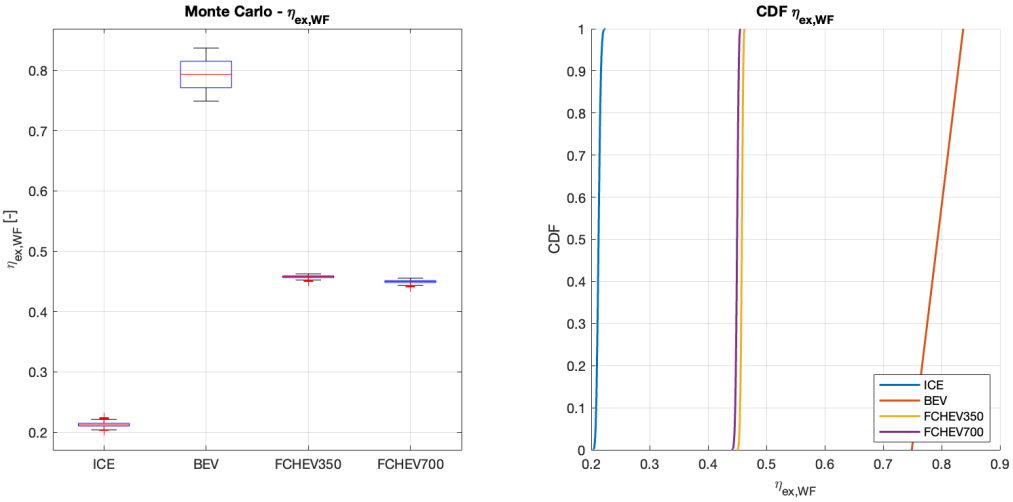

Figure 13: Monte Carlo distribution and CDF of $\eta_{\mathrm{ex,WF}}$ (Duty cycle 1).

The distributions confirm the ranking observed in the deterministic analysis. The BEV configuration shows the highest efficiency but also a wider spread, reflecting its sensitivity to upstream electricity assumptions. In contrast, the FCHEV configurations exhibit narrower distributions, indicating a more stable performance with respect to parameter uncertainty. The ICE configuration remains consistently characterized by low efficiency and limited variability.
The Monte Carlo results for total GHG emissions are shown in Fig. 14.

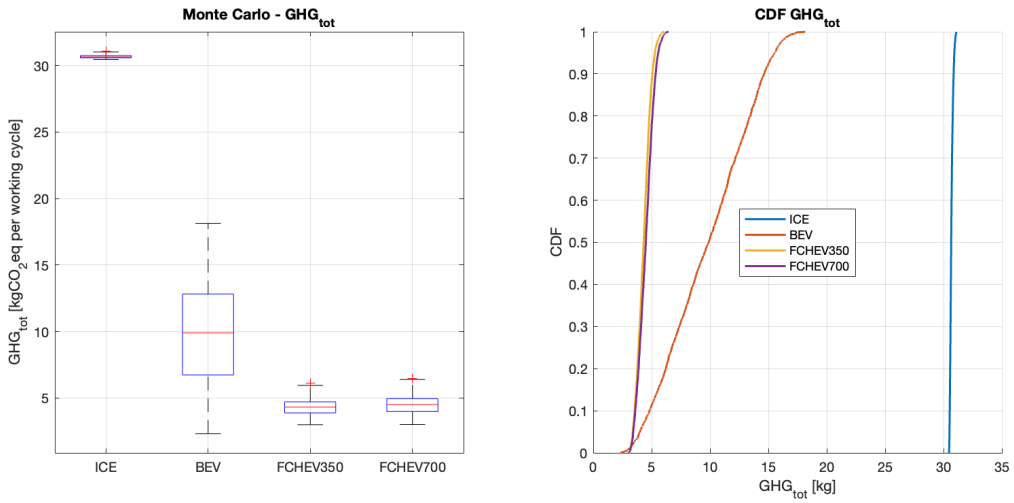

Figure 14: Monte Carlo distribution and CDF of total GHG emissions (Duty cycle 1).

The ICE configuration remains clearly separated from the other architectures, with consistently high emissions and negligible overlap with alternative solutions. The BEV shows a wider distribution, reflecting its dependence on the electricity mix and on the embodied assumptions. The FCHEV configurations maintain low and relatively stable emissions, confirming their robustness under the selected hydrogen pathway.
A further analysis is performed by considering different hydrogen production pathways, as shown in Fig. 15 for the FCHEV350 case.

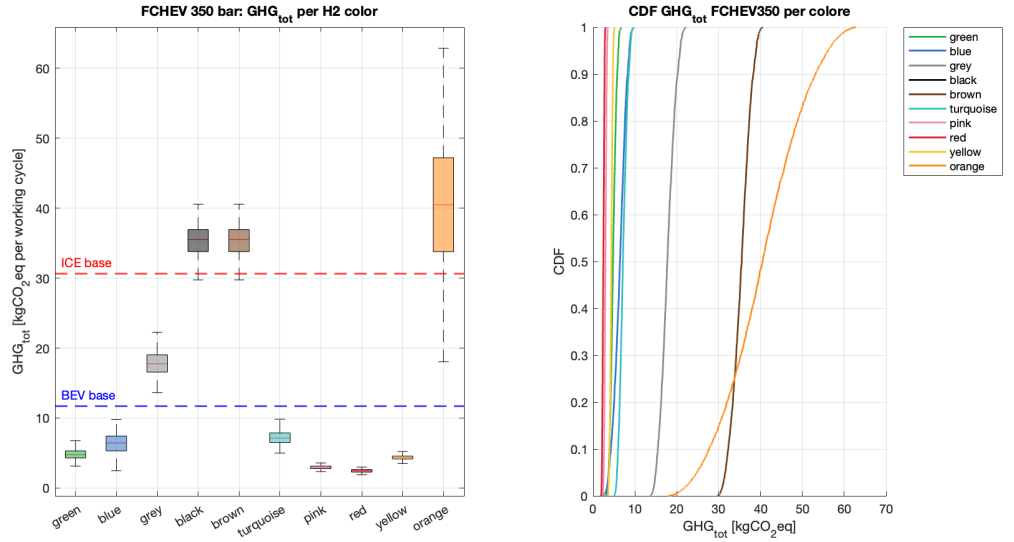

Figure 15: GHG emissions distribution for FCHEV350 under different hydrogen production pathways (Duty cycle 1).

The results highlight the strong dependence of hydrogen-based configurations on the upstream production pathway. Low-carbon pathways such as green, pink and red hydrogen lead to emissions significantly lower than both the BEV and the ICE baselines. Conversely, carbon-intensive pathways (grey, black, brown) result in emissions comparable to, or even exceeding, those of the diesel configuration. This analysis demonstrates that the environmental advantage of hydrogen technologies is not intrinsic, but strictly conditional on the decarbonization of hydrogen production. The variability observed across pathways also explains the dispersion observed in the Monte Carlo analysis, particularly for hydrogen-based systems.
Overall, the results confirm that while BEV architectures maximize thermodynamic efficiency, hydrogen-

based solutions offer competitive environmental performance under low-carbon supply conditions and provide advantages in terms of energy density and operational flexibility. The use of real-world duty cycles, representative of shredding, treatment and soil tillage operations, ensures that the results are directly applicable to practical agricultural scenarios. This well-to-field task-based approach allows capturing both traction- and implement-driven energy requirements, overcoming the limitations of conventional on-road driving-cycle analysis.

7. Conclusions

This study presented an integrated thermodynamic and environmental assessment of alternative powertrain architectures for agricultural tractors, combining energy analysis, exergy-based metrics, and life cycle considerations under realistic field operating conditions.

The use of representative agricultural duty cycles, derived from real operations such as shredding, treatments, and soil tillage, allowed capturing the combined effects of traction and implement-driven loads. This approach provides a more meaningful evaluation compared to conventional on-road driving cycles, particularly for machinery where PTO demand plays a dominant role.

From a thermodynamic perspective, the BEV configuration consistently exhibits the highest exergy efficiency, with tank-to-field values approaching 0.9 and well-to-field values around 0.8. This result is primarily due to the direct use of electrical energy and the absence of intermediate conversion processes. In contrast, the FCHEV architectures show intermediate efficiencies (approximately 0.44–0.47), reflecting the additional hydrogen-to-electricity conversion step, while the ICE configuration remains significantly penalized by combustion irreversibilities, with efficiencies below 0.25.

The comparison between hydrogen storage at 350 and 700 bar highlights a clear trade-off between system compactness and upstream energy demand. While the 700 bar configuration enables a reduction in storage volume of about 40%, it requires higher compression work and refuelling energy, resulting in a slight decrease in overall exergy efficiency. However, the impact on useful exergy output remains negligible, indicating that the choice between storage pressures is mainly driven by packaging and infrastructure considerations.

From an environmental perspective, the ICE architecture exhibits the highest greenhouse gas emissions, dominated by the operational phase. The BEV configuration significantly reduces operational emissions, but its total impact is influenced by the embodied contribution of the battery system. The FCHEV configurations achieve the lowest emissions under the green hydrogen scenario, with a more balanced distribution between operational and manufacturing contributions.

The analysis of different hydrogen production pathways confirms that the environmental performance of FCHEV systems is strongly dependent on the upstream carbon intensity. While low-carbon pathways (e.g., green, pink, or red hydrogen) enable substantial emission reductions, carbon-intensive routes can offset or even negate the environmental benefits compared to conventional diesel systems. This highlights that hydrogen-based solutions are not intrinsically sustainable, but conditional on the decarbonization of the supply chain.

Uncertainty analysis based on Monte Carlo simulations demonstrates the robustness of the main trends. The BEV architecture shows higher sensitivity to electricity-related assumptions, while FCHEV systems exhibit more stable behavior under the selected parameter ranges. The ICE configuration remains consistently characterized by high emissions and low efficiency, with limited variability.

Overall, the results indicate that BEV architectures maximize thermodynamic efficiency, whereas FCHEV systems can achieve superior environmental performance under low-carbon hydrogen supply conditions, while offering advantages in terms of energy density and operational flexibility. The ICE configuration remains the least favorable option both thermodynamically and environmentally.

Future work will focus on the integration of renewable energy systems at farm level, including on-site hydrogen production and storage, as well as the development of advanced energy management strategies. In this context, the proposed framework provides a robust basis for coupling tractor operation with hybrid energy systems and for supporting the design of next-generation sustainable agricultural

machinery.

References

[1] Salvatore Martelli, Valerio Martini, Francesco Mocera, and Aurelio Somà. Life cycle assessment comparison of orchard tractors powered by diesel and hydrogen fuel cell. *Energies*, 17:4599, 2024.

[2] Marco Maggini, Gabriele Loreti, Francesca Santoni, Andrea L. Facci, Stefano Ubertini, Viviana Cigolotti, and Giulia Monteleone. Technical assessment and economic analysis of zero-carbon freight road transportation vehicles. *International Journal of Hydrogen Energy*, 212:153707, 2026.

[3] Valerio Martini, Francesco Mocera, and Aurelio Somà. Numerical investigation of a fuel cell-powered agricultural tractor. *Energies*, 15:8818, 2022.

[4] Mert Ozsaban, Adnan Midilli, and Ibrahim Dincer. Exergy analysis of a high pressure multistage hydrogen gas storage system. *International Journal of Hydrogen Energy*, 36:11440–11450, 2011.

[5] Qian Cheng, Ruiqiang Zhang, Zhusheng Shi, and Jianguo Lin. Review of common hydrogen storage tanks and current manufacturing methods for aluminium alloy tank liners. *International Journal of Lightweight Materials and Manufacture*, 7:269–284, 2024.

[6] Evangelos Tzimas, Christos Filiou, Stamatis D. Peteves, and Jean-Baptiste Veyret. *Hydrogen Storage: State-of-the-Art and Future Perspective*. EUR 20995 EN. European Commission, Joint Research Centre, 2003.

[7] David R. Morris and Jan Szargut. Standard chemical exergy of some elements and compounds on the planet earth. *Energy*, 11(8):733–755, 1986.

[8] Guohui Song, Jun Xiao, Hao Zhao, and Laihong Shen. A unified correlation for estimating specific chemical exergy of solid and liquid fuels. *Energy*, 40:164–173, 2012.

[9] Barbara Mendecka, Laura Tribioli, Simone Lombardi, and Gino Bella. Exergo-environmental analysis of full-electric tractor under real-world operating conditions. In *Proceedings of the 38th International Conference on Efficiency, Cost, Optimization, Simulation and Environmental Impact of Energy Systems (ECOS)*, Paris, France, 2025.

[10] D. Stock and R. Bauder. The new audi 5-cylinder turbo diesel engine: The first passenger car diesel engine with second generation direct injection. *SAE Technical Paper*, 1990.

[11] Danfoss. Electric motors and generators. `https://powersource.danfoss.com/products/electric-converters-motors-and-systems/electric-motors-and-generators/p/18310?tab=documents`, 2026. Accessed: 2026-04-18.

[12] Ballard Power Systems. Ballard power systems. `https://www.ballard.com/`, 2026. Accessed: 2026-04-18.

[13] J.Y. Wong. *Theory of ground vehicles*. John Wiley & Sons, 2008.

[14] B. Mendecka, L. Tribioli, S. Lombardi, L. Federici, et al. Environmental impacts of a low-profile full electric specialized tractor: A case study on different battery pack configurations. In *SAE Technical Paper*, number 2024-01-4318, 2024.

[15] Massimo Cecchini, Barbara Mendecka, Gianmarco Rigon, Danilo Monarca, Davide Gattamelata, Leonardo Vita, Daniele Puri, Luciano Ortenzi, Davide Facchinetti, Lavinia Eleonora Galli, Gino Bella, and Domenico Pessina. Compact tractor 4.0: An investigation for the development of a low-profile full electric specialized tractor. In Remigio Berruto, Marcello Biocca, Eugenio Cavallo, Massimo Cecchini, Sabina Failla,

and Elio Romano, editors, *Safety, Health and Welfare in Agriculture and Agro-Food Systems*, pages 172–185, Cham, 2024. Springer Nature Switzerland.

[16] Jan Szargut, David R. Morris, and Frank R. Steward. *Exergy Analysis of Thermal, Chemical, and Metallurgical Processes*. Hemisphere Publishing Corporation, New York, 1988.

[17] Maarten L. Neelis, Henk J. van der Kooi, and Hans J. C. Geerlings. Exergetic life cycle analysis of hydrogen production and storage systems for automotive applications. *International Journal of Hydrogen Energy*, 29:537–545, 2004.

[18] Alen Murat Kuyumcu, Barış Bingül, and Fırat Akar. Well-to-wheel carbon footprint and cost analysis of gasoline, diesel, hydrogen ice, hybrid and fully electric city buses. *Energy*, 301:131685, 2024.

[19] SAE International. Sae j2601: Fueling protocols for light duty gaseous hydrogen surface vehicles. SAE Standard J2601, 2020. Hydrogen fueling protocol for 35 MPa and 70 MPa gaseous hydrogen vehicles.

[20] SAE International. Sae j2601/2: Fueling protocol for gaseous hydrogen powered heavy duty vehicles. SAE Standard J2601/2, 2023. Fueling protocol for 35 MPa gaseous hydrogen heavy-duty vehicles.

[21] Amgad Elgowainy, Krishna Reddi, Dong-Yeon Lee, Neha Rustagi, and Erika Gupta. Techno-economic and thermodynamic analysis of pre-cooling systems at gaseous hydrogen refueling stations. *International Journal of Hydrogen Energy*, 42(49):29067–29079, 2017.

[22] Jimena Incer-Valverde, Amira Korayem, George Tsatsaronis, and Tatiana Morosuk. “Colors” of hydrogen: Definitions and carbon intensity. *Energy Conversion and Management*, 291:117294, 2023.

[23] Yiling Xiong, Fang Wang, Dongchang Zhao, Xia Sun, Feng Ren, Ming Zhao, Jiming Hao, Yaling Wu, and Shiqiu Zhang. Cradle-to-gate ghg emissions and decarbonization potentials of minivan-equipped hydrogen fuel cell system. *Resources, Conservation and Recycling*, 212:107877, 2025.

ACKNOWLEDGEMENT

This research was conducted within the framework of the HyAgroBox project (Project Code: MI-RNP-00178), funded by the Italian Ministry of Environment and Energy Security (MASE) under CUP F53C25001640001, within the Mission Innovation framework.